Nano Research
Open Access
Research Article

Study on the linear dynamic range and anti-background light interference of n-Si/n-ZnO heterojunction photodetectors enhanced by transient current

Yongle Zhang, Xue Feng, Feng Yang, Yingfeng Duan, Yuwei Zhao, Tuo Chen, Peng Wang, Junmeng Guo, Zuliang Du, and Gang Cheng ✉

Key Lab for Special Functional Materials of Ministry of Education, School of Nanoscience and Materials Engineering, Collaborative Innovation Center of Nano Functional Materials and Applications, Henan University, Kaifeng 475004, China

Cite this article: *Nano Research*, **2025**, *18*, 94907007. https://doi.org/10.26599/NR.2025.94907007

ABSTRACT: The self-powered photodetectors (PDs) have gained much attention due to they do not require additional external energy and can be well applied in distributed optoelectronic detection networks. However, the small built-in electric field and rich interface states of self-powered PDs, make it a severe challenge to achieve large linear dynamic range (LDR) and high responsivity. Herein, a n-Si/n-ZnO heterojunction structure self-powered PD is constructed, fully utilizing the characteristics of transient current less affected by the excitation power and interface states, and using transient current as the detection signal significantly improves the PD's photocurrent responsivity (R) and the LDR. Under the excitation of 365, 530, 660 and 970 nm light, the device's maximal peak-to-peak transient current responsivity ($R_{tt'}$) values are 89.3, 341, 439 and 542 mA·W^{-1}. The device's corresponding LDR is 113.8, 112.5, 105.9 and 74.6 dB, which are 25.9, 29.9, 20.3 and 14.4 dB higher than steady-state current (I_s), respectively. Furthermore, in the presence of background light, the device's transient current exhibits enhanced light intensity change resolution and background light interference resistance. Finally, the 6 × 6 detector array's transient current (I_t) response has a good consistency and LDR, which significantly improves the device's imaging quality and resolution. This work provides new ideas for improving the R and LDR of self-powered PDs, and will promote the development and application of transient current responsive self-powered PDs in the fields of high-sensitivity detection and fast imaging.

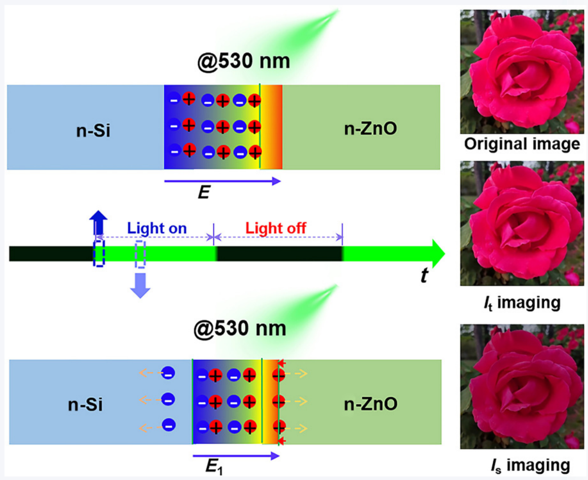

KEYWORDS: n-Si/n-ZnO heterojunction photodetectors, linear dynamic range, anti-background light interference, transient current, wide spectrum response characteristic

1 Introduction

With the rapid development of new-generation information technologies such as the Internet of Things, big data and artificial intelligence, the demand for the speed and quality of information collection, transmission and processing continues to increase [1–3]. Photodetectors (PDs) are the basic units for photoelectric sensing, imaging and the Internet of Things, and their performance determines the speed and quality of data collection [4–7]. Therefore, the development of new high-performance PDs with low power consumption, high detection sensitivity, high detection speed and good environmental adaptability has attracted extensive attention from researchers [8–10]. The linear dynamic range (LDR) of optical power (or light intensity) is an important performance of the PD, which determines the imaging quality of the detector [11, 12]. Traditional metal oxide semiconductor technology has a dynamic response range of only 70 dB [12], which is significantly less than the 280 dB dynamic range of natural light intensity [13]. The detection and imaging of devices are significantly impacted by the limited spectral LDR. To increase the LDR of PDs, researchers

Received: June 13, 2024; **Revised:** August 11, 2024
Accepted: August 26, 2024

✉Address correspondence to chenggang@henu.edu.cn

have adopted methods such as controlling optical aperture, liquid lens, adjusting exposure time and utilizing algorithmic post-processing [14–16]. However, these methods typically require complex hardware and software resources. Recently, devices with visual adaptive capabilities have been able to improve the dynamic response range of optical power and reduce hardware complexity [13]. For example, gate voltage-regulated MoS_2 transistors [13], $CsPbBr_3$/two-dimensional (2D) MoS_2 heterojunctions [17, 18] and complementary bulk heterojunction (BHJ) transistors, etc [19]. However, the devices of the above strategies usually require external voltage driving or gate voltage regulation of device performance, which increases the energy consumption of the device. The LDR of a device's optical power can be greatly increased by using novel materials like perovskite materials [20–22] and two-dimensional materials [13, 23–25]. However, the stability, adaptability and preparation process of new material devices still face some challenges, which restrict their application in high-speed detection and imaging.

Heterojunction PDs with self-powered characteristics do not require additional external energy, and can be well applied in distributed optoelectronic detection networks and the Internet of Things [9, 26–28]. This structural device can also satisfy the demands of high-speed detection and imaging because of its quick responsiveness feature. Especially recently, using the transient current generated by devices when it is light-excited or turned off as a detection signal can effectively increase the photoelectric responsivity and response speed of photoelectric detection without changing the device structure [29–31]. For example, significant improvements in device response performance were achieved in p-Si/n-ZnO heterojunctions [29, 32, 33], Si/NiO/ZnO heterojunctions [34], ZnO/SnS heterojunctions [35], ZnO/$ZnTe_2$ hetero-junctions [36]and Si/SnS heterojunctions [37]. Additionally, using transient photocurrent as the detection signal can increase the environmental and temperature adaptability of the PD [28, 29, 38]. The LDR of optical power (light intensity) of PDs is an important performance of PDs. However, to our knowledge, there are currently no research reports on the enhancement of the LDR of device optical power by transient photocurrent. The reason for this phenomenon may be due to the different transient photocurrent response characteristics of n–n heterojunction and p–n heterojunction, while most previous studies were based on p–n heterojunction. Additionally, the photoelectric performance of devices in the absence of background light is usually studied, while real devices typically operate in environments with background light. The impact of background light interference on the photoelectric response performance of devices is rarely reported. Therefore, studying the LDR of the device' s transient photocurrent and exploring the ability of transient current to resist background light interference is of great significance for achieving high-speed photoelectric detection and imaging of distributed signals in complex environments.

This article constructs an n-Si/n-ZnO heterojunction structure self-powered PD, using transient current as the detection signal to significantly improve the photocurrent responsivity and LDR of the PD. Under the excitation of 365, 530, 660 and 970 nm wavelength light, the device's maximal peak-to-peak transient current responsivity ($R_{tt'}$) values are 89.3, 341, 439 and 542 mA·W^{-1}, respectively. They are 6.6, 15.6, 9.7 and 7.5 times higher than the responsivity of the I_s (R_s), respectively. The LDR of the device's transient current (I_t) is 113.8, 112.5, 105.9 and 74.6 dB, which are 25.9, 29.9, 20.3 and 14.4 dB higher than steady-state current (I_s), respectively. Secondly, the effect of background light on the optoelectronic response performance of the device is studied. The results show that transient current has a higher resolution of light intensity changes and resistance to light intensity interference. Under 530, 660 and 970 nm wavelength light excitation, the maximum relative responsivity ($R'_{tt'}$) of the device is 428.8, 601.5 and 621.7 mA·W^{-1}, respectively. Under 530, 660 and 970 nm light excitation, when the power density of the background light is 30 times that of the variable light pulse power density, the peak-to-peak current relative responsivity retention factors of the device are 0.61, 0.59 and 0.61, respectively, which are 41.9%, 22.9% and 68.1% higher than the steady-state current relative responsivity retention factors, respectively. Finally, a 6 × 6 detector array was constructed to investigate the imaging effect of array devices on 530 nm wavelength light, and the results show that using the device's I_t as the detection signal significantly improved the imaging quality and resolution of the device. This work provides new ideas for improving the responsivity and the LDR of photocurrent and will promote the development and application of transient current responsive self-powered PDs in fields like high sensitivity detection and rapid imaging.

2 Experimental

2.1 Preparation of devices

The 500 μm n-type silicon wafer (with a crystal surface (100) and a resistivity of 10–20 Ω· cm) was cleaned by ultrasonic cleaning with ethanol and deionized water, and dried with nitrogen gas. Firstly, a layer of ZnO thin film (approximately 50 nm) was sputtered on the Si surface as a seed layer using magnetron sputtering (75PRO line, power 80 W, sputtering time 25 min). Secondly, the sample with ZnO seed layer was placed into a mixed solution containing 30 mM $Zn(NO_3)_2$, 30 mM hexamethylenetetramine (HMTA) and 1.6% ammonia by volume 62.5 mL to grow ZnO nanowire arrays. The reaction temperature was 90 °C and the reaction time was 120 min. Then, deionized water was used to clean the residual reaction solution on the ZnO nanowire array, and let the sample dry naturally in air. Finally, a layer of indium tin oxide (ITO) thin film was sputtered at the end of ZnO nanowires using magnetron sputtering as the upper electrode, and 10 nm chromium and 50 nm gold thin films were evaporated on Si wafers using electron beam evaporation (DZS-500) as the bottom electrode. The upper and bottom electrodes were connected to the test electrode through silver adhesive bonding wires. The preparation process of array devices was similar to the above, where 6 × 6 polyethylene terephthalate (PET) mask plates were placed above the device before sputtering the ITO electrode.

2.2 Material characteristics

The microstructure and crystal type of ZnO were characterized by field emission scanning electron microscopy (FESEM, JEOL JSM-7610F Plus) and X-ray diffraction (XRD) analyzer (D8-ADVANCE), respectively.

2.3 Optical and electrical measurements

The absorption of ZnO and Si materials was measured using a ultraviolet-visible (UV–Vis)–near infrared spectrophotometer (PE Lambda 950), where ZnO nanowire arrays were grown on quartz substrates and measured using the transmission method, while Si sheets were measured using reflection method. Current–voltage

(I–V) and capacitance–voltage (C–V) of the devices were measured using a semiconductor analyzer (Keithley 4200-SCS). The transient current–time (I–t) and voltage–time (V–t) characteristics of the device were measured through a built optoelectronic measurement system, including a software-controlled sensitive ammeter (SR570) data acquisition card (USB-6361). The light sources at 365, 530, 660 and 970 nm wavelengths used in the experiment were provided by light-emitting diode (LED) fiber couplers (Thorlabs M365FP, M530F2, M660FP1 and M970F3) and controlled by LED drivers (Thorlabs DC2200). Finally, they were irradiated onto the sample through fiber coupling. The size of the optical power density, the current with or without background light passing through the driver, and the broadband filter were precisely controlled. The measurement of corresponding optical power density was measured using a power meter (Thorlabs PM 320E). The sample was placed at room temperature and atmospheric pressure on the probe table (CRYOX80).

3 Results and discussion

Figure 1(a) is a schematic diagram of the structure of n-Si/n-ZnO devices (the detailed preparation process of the device can be found in the experimental section). Figure 1(b) is the SEM image of ZnO nanowires grown by the hydrothermal method. From the top view, it can be seen that there are several nanowires arranged in a columnar structure. The nanowire vertical substrate grows preferentially along the [002] direction (Fig. S1(c) in the Electronic Supplementary Material (ESM)). From the side view SEM image of Si/n-ZnO devices, it can be seen that ITO has a thickness of over 200 nanometers and is wrapped around ZnO nanowires (in the illustration of Fig. 1(b) and Fig. S3 in the ESM). The energy band diagrams of various materials used to construct the device are shown in Fig. 1(c). The valence band positions of ZnO and Si relative to the vacuum energy levels are −7.71 and −5.22 eV, respectively [29, 39, 40]. According to the absorption curves of ZnO and Si materials, the band gaps of ZnO and Si materials are 3.2 and 1.13 eV, respectively (Figs. S1(a) and S1(b) in the ESM). According to the absorption spectrum of ZnO material, the high photoluminescence intensity corresponding to the 450–650 nm wavelength band indicates that the ZnO nanowires obtained by the hydrothermal method have rich defect states (Fig. S1(d) in the ESM) [33, 41]. From the I–V curve of the device, it can be seen that the formed n-ZnO/n-Si device has good rectifying characteristics (illustrated in the device measurement diagram), indicating that the ZnO and Si interfaces have good contact to form a heterojunction (Fig. 1(d)). At a bias of ±1 V, the rectification ratio of the device's current is approximately 1:68.8. According to the I–V curve in the exponential coordinate system, the current transport of the device under negative bias can be divided into four regions with the increase of negative bias: generation recombination current region, diffusion current region, large injection region and series resistance effect region [42].

The device's I–V curves at various 530 nm light excitation power densities are displayed in Fig. 1(e). During forward bias, the current of the device varies less with the optical power density, while during reverse bias, the current of the device increases rapidly with the increase of reverse bias voltage. As the optical power density increases, the current of the device at reverse bias increases rapidly. Figure 1(f) displays the device's I–t curves at various 530 nm light excitation power densities with a 20 Hz excitation frequency. Within a single pulse cycle, the device's I–t curve displays four distinct response processes (Fig. S4(a) in the ESM). The corresponding currents are the transient current (I_t) at the switching moment, the steady-state current response (I_s), the transient current response ($I_{t'}$) at the turning-off moment, the current returning to the dark state ($I_{s'}$), and peak-to-peak transient current ($I_{tt'} = I_t - I_{t'}$). As the power density of the excitation light increases, the current for each device process increases. Among them, I_t and $I_{t'}$ are more significant increases, which provides favorable conditions for improving the photoelectric response of the device at higher power density.

The current response of the device remains linear over a large power density range with excitation power density, which is of great significance for both optoelectronic detection and imaging. Figure

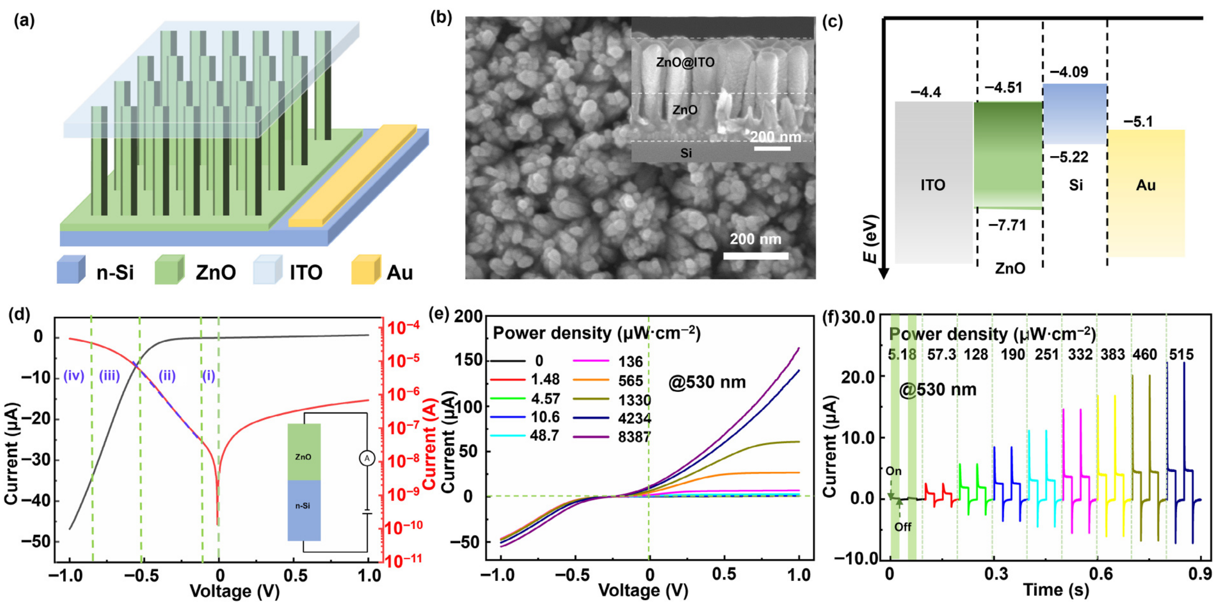

Figure 1 (a) Schematic diagram of an n-Si/n-ZnO device. (b) SEM image of ZnO nanowire array (illustrated as a cross-sectional view of n-Si/n-ZnO device). (c) Energy band diagrams of various materials that make up the device. (d) The device's I–V characteristic curve in the dark condition. ((e) and (f)) The device's (e) I–V and (f) I–t curves at various power densities during 530 nm light excitation.

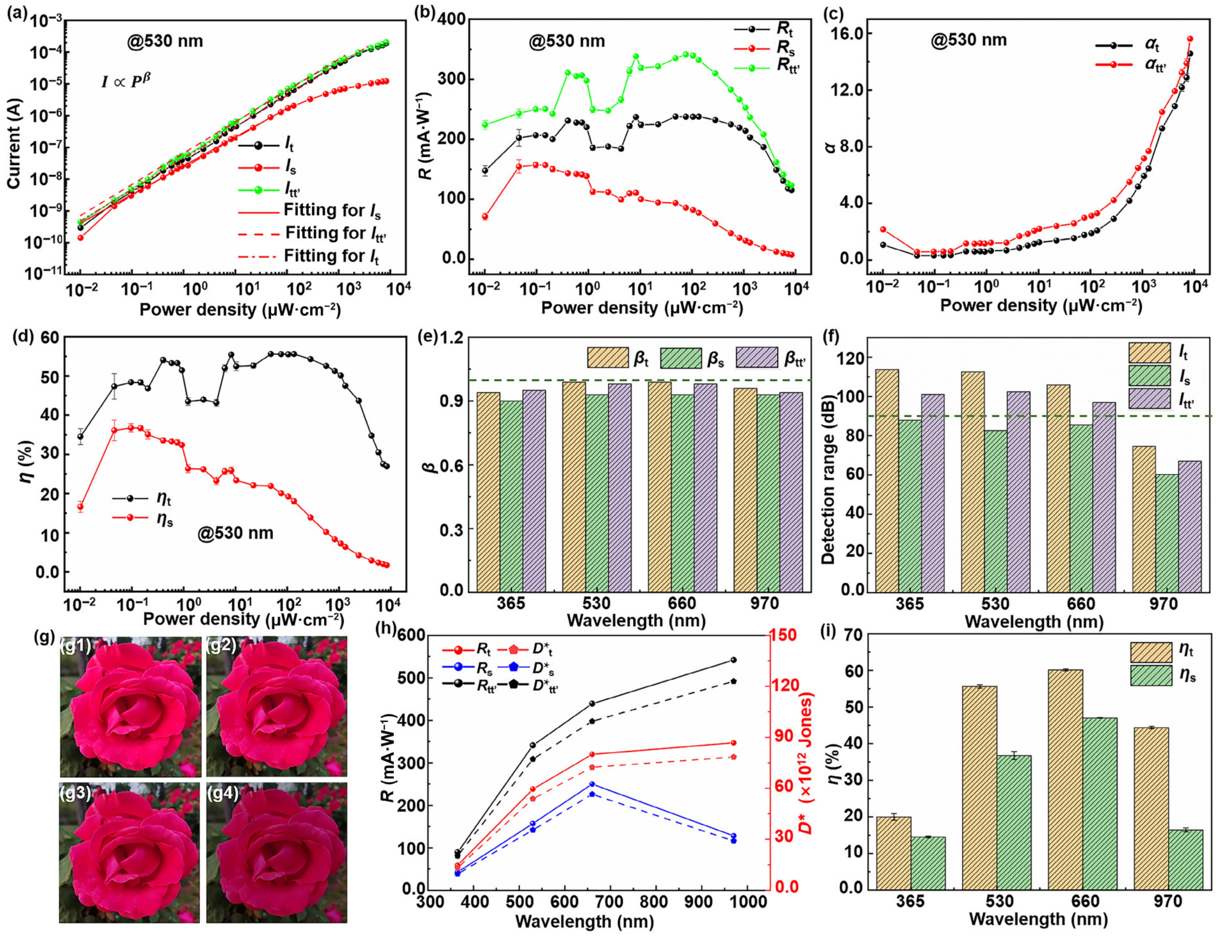

Figure 2 The characteristics of the device's photoelectric response to light pulse excitation in the absence of ambient light. ((a)–(d)) The relationship curve between the (a) current, (b) responsivity, (c) enhancement factor and (d) external quantum efficiency of the device and the excitation light power density under 530 nm wavelength light excitation. (e) The current linear factor and (f) linear response range the device under various wavelengths of light excitation. (g) Imaging effect of the device's various process currents (where (g1) is the original image, and (g2)–(g4) respectively simulates the imaging of I_t, $I_{tt'}$ and I_s of the device). (h) The maximum current responsivity, specific detectivity and (i) external quantum efficiency of the device under different wavelengths of light excitation. The error bar is obtained from the 5 data.

2(a) shows the relationship curve of the device's I_t, I_s and $I_{tt'}$ with variations in optical power density. In the double logarithmic coordinate system, the device's I_t, I_s and $I_{tt'}$ all monotonically linearly increase with an increase in excitation optical power density (P) when P < 135 μW·cm⁻², with corresponding slopes of 0.99, 0.93 and 0.98, respectively. This indicates that using I_t and $I_{tt'}$ as optical detection signal devices has better linearity with the increase of optical power density. However, as power density increases, the device's I_s, I_t and $I_{tt'}$ all gradually deviate from linearity, with corresponding power densities of 135.3, 4234 and 1314 μW·cm⁻², respectively. The device's current responsivity can be described as [43, 44]

$$R = (I_{light} - I_{dark})/P_{ill} \quad (1)$$

where I_{light} and I_{dark} are the photocurrent and dark current of the self-powered PD, respectively. P_{ill} is the effective excitation optical power, and the R_t, R_s and $R_{tt'}$ are the responsivity of the I_t, I_s and $I_{tt'}$, respectively. As the power density increases, the device's R_t, R_s and $R_{tt'}$ show an increasing and then decreasing law (Fig. 2(b)). When the R_t, R_s and $R_{tt'}$ of the device begin to decrease, there is also a significant difference in the corresponding optical power density, which is 829.3, 0.097 and 76.6 μW·cm⁻², respectively. To describe the enhancement effect of transient current relative to steady-state current, the current enhancement factor (α) can be expressed as [45]

$$\alpha = I/I_s - 1 \quad (2)$$

the α_t and $\alpha_{tt'}$ are the enhancement factor of I_t and $I_{tt'}$, respectively. The device's α_t and $\alpha_{tt'}$ first slowly increase with the power density, and then rapidly increase (Fig. 2(c)). To better characterize the detection ability of PDs, the specific detectivity is defined as [29]

$$D^* = R/(2eI_{dark}/S)^{0.5} \quad (3)$$

where S is the effective area of the device, e is the electronic charge. D_t^*, D_s^* and $D_{tt'}^*$ are the specific detectivity of the device's I_t, I_s and $I_{tt'}$, respectively. Due to the formation of a good heterojunction between Si/ZnO, it can effectively improve the photoelectric response characteristics of the device and suppress the dark current response of the device. The device has high responsivity and specific detectivity, the maximum $R_{tt'}$ and $D_{tt'}^*$ are 341 mA·W⁻¹ and 7.72 × 10¹³ Jones, respectively (Fig. S5 in the ESM). The external quantum efficiency (η) of the device is defined as

$$\eta = Rhv/e \quad (4)$$

where v is the frequency of the light wave and h is the Planck constant. η_t and η_s are external quantum efficiencies corresponding to the device's R_t and R_s, respectively. The device's η_t and η_s show a decreasing trend with the increase in power density (Fig. 2(d)), and the corresponding maximum η_t and η_s are 55.6% and 36.8%, respectively.

The Si/ZnO heterojunction, as a broad-spectrum PD, has good response characteristics to both ultraviolet and near-infrared light (Figs. S6–S9 in the ESM). The relationship between the device's photocurrent response and the optical power density can be expressed as [46]

$$I = AP^{\beta} \quad (5)$$

where I is the device's photocurrent, A is the coefficient, P is the excitation power density, and β is the linear factor of current response. β_t, β_s and $\beta_{tt'}$ represent the linear response factors of I_t, I_s and $I_{tt'}$, respectively. Under different wavelengths of light excitation, the device's β_t, β_s and $\beta_{tt'}$ are all more than 0.9, and the device's β_t is highest and β_s is lowest (Fig. 2(e)). This further indicates that using the device's I_t as a detecting signal can improve the device's light intensity resolution. Both device's β_t and β_s have significant wavelength-dependent characteristics. The device's β_t are 0.94, 0.99, 0.99 and 0.98 under the excitation of 365, 530, 660 and 970 nm wavelength light, and the corresponding β_s are 0.9, 0.93, 0.93 and 0.93, respectively. The LDR of the PD is defined as [21, 25]

$$\text{LDR} = 20\log(P_{\max}/P_{\min}) \quad (6)$$

where $P_{\max}$ and $P_{\min}$ are the maximum and minimum optical power density of photocurrent deviation from linearity, respectively. Based on the device's I_s response, the LDR of the device is less than 90 dB under different wavelength light responses (Fig. 2(f)). The maximum LDR of the device under 365 nm wavelength light excitation is 87.9 dB. Due to the limitation of the lowest power density excited by the device, the LDR of the corresponding device may be underestimated. Using the device's I_t and $I_{tt'}$ as detection signals can effectively improve the LDR of the device. Under the excitation of 365, 530, 660 and 970 nm light, the LDR of the device with I_t as a detection signal is 113.8, 112.5, 105.9 and 74.6 dB, respectively, which is 25.9, 29.9, 20.3 and 14.4 dB higher than that with I_s as a detection signal and its performance is comparable to that of commercial devices (Table S2 in the ESM). The difference in LDR of devices under different wavelengths of light excitation may be influenced by the distribution of photo-generated carriers within the material.

To intuitively demonstrate the importance of the linear factor of the device's optical power in imaging, the changes in brightness and contrast of the image after detecting the imaging with different responsiveness linear factors using software simulation are shown in Fig. 2(g). Figure 2(g1) shows the original image of China rose, while Figs. 2(g2)–2(g4) show β taking 0.99, 0.98 and 0.93, the corresponding photocurrent is used as the output simulation diagram. The brightness and contrast of the output image vary with β increasing indicating a high β (close to 1) has important applications in the field of optoelectronic detection and imaging. Figure 2(h) shows the maximum values of the responsivity and specific detectivity of the device under various wavelengths of light excitation. The device's R_s first increases and then decreases with the increase of wavelength, which is consistent with the absorption characteristics of the material (Fig. S1(b) in the ESM). However, the device's R_t and $R_{tt'}$ monotonically increase with the increase of wavelength. Using transient current as a detection signal can effectively improve the performance of the device. When the excitation wavelengths are 365, 530, 660 and 970 nm, the maximum values of $R_{tt'}$ are 89.3, 341, 439 and 542 mA·W^{-1}, and the corresponding $D_{tt'}$* are 2.02×10^{13}, 7.72×10^{13}, 9.94×10^{13} and 1.23×10^{14} Jones, respectively. The influence of Si and ZnO material's reflection and absorption characteristics, the devices's η_s at 365 and 970 nm are only 14.5% and 16.4%, respectively (Fig. 2(i)). When using I_t as the detection signal, the device's η_t under various wavelength light excitation is 20.0%, 55.6%, 60.1% and 44.3%, respectively, reaching a high level.

The actual working conditions of devices often have background light, exploring the light detection ability and resolution of devices under background light is of great significance for expanding the application scenarios of PDs. The device exhibits a significant transient current response at the moment of optical power change (Fig. 3(a)). However, when there is background light, the high steady-state current noise of the device will affect the resolution of the device's optical detection. When the optical power density increases (decreases), the device generates a forward (reverse) transient current spike response (Fig. 3(b)). By utilizing the high sensitivity of transient current response to changes in light intensity, it is possible to detect changes in light intensity in the environment with high sensitivity. Under the cycle the excitation of 5.1 ± 0.5 μW·cm^{-2}, 530 nm wavelength light, the absolute values of the device's I_t, I_s, $I_{s'}$ and $I_{t'}$ monotonically increase with the increase of background light excitation power density (Fig. 3(c)). To characterize the effect of increasing background light power density on the device's optical responsivity, each current's relative responsivity of the device under background light conditions is $R'_{tt'}$, $R'_{ts'}$, $R'_{ss'}$ and $R'_{st'}$, respectively. The device's $R'_{tt'}$, $R'_{ts'}$, $R'_{st'}$ and $R'_{ss'}$ show a rule of slowly decreasing with the increase of background light power density (Fig. 3(d)). The device's enhancement factor (α') and external quantum efficiency (η') as the background light power density monotonically increases (Fig. S12(b) in the ESM) and decreases (Fig. S12(c) in the ESM), respectively.

As a detector with a wide spectral response, the device's $R'_{tt'}$, $R'_{ts'}$, $R'_{ss'}$ and $R'_{st'}$ first rapidly increase, and then tend to saturate with increasing wavelength (Fig. 3(e)). Under the condition of background light, the device has almost the same current response $R'_{ts'}$ and $R'_{st'}$ at the moment of switching light. Except at a wavelength of 365 nm, the maximum relative photocurrent responsivity of the device has been improved to some extent in the presence of background light. This may be because the photo-generated carriers generated under background light can partially neutralize the defect state, reducing the probability of the material's defect state capturing the newly generated photo-generated carriers when excited by pulsed light. Additionally, the photo-generated carriers generated by background light can effectively reduce the resistance of the device. The combined effect of the above two improves the device's photoelectric current responsivity. Utilizing the transient current response generated by switching light as the detection signal, the device has a high η' (Fig. 3(f)). Under the excitation of 530 and 660 nm wavelength light, the device's η'_t values are 63.3% and 69.7%, respectively. By treating the surface of the material and increasing the absorption of the material and device, the device's η' can be further improved.

To characterize the current response ability of various parts of the device to resist interference from background light, we define the photocurrent retention factor (η'') of the device as

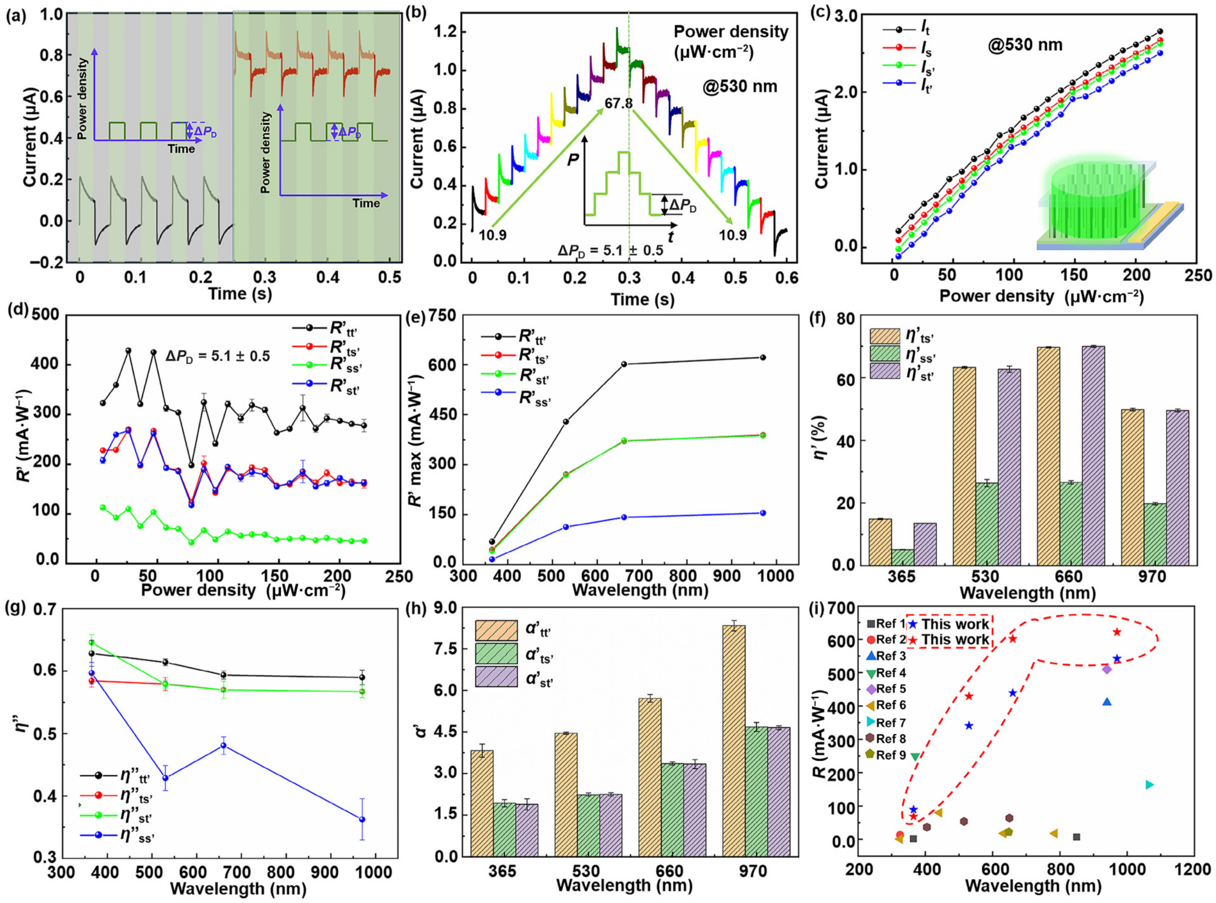

Figure 3 The photoelectric response characteristics of the device under light pulse excitation when there is background light. (a) The device's *I*–*t* curve without background light and 10 times excitation power density ($P/\Delta P_D = 10$) under excitation of 20 Hz, 5.1 μW·cm⁻², 530 nm light (ΔP_D is the change in optical power density). (b) Maintain excitation light power of 5.1 μW·cm⁻², the *I*–*t* curve of the device with background light power density increases and decreases. ((c) and (d)) The relationship curve between the (c) current and (d) relative responsivity of each process of the device and the background light power density. (e) The maximum relative responsivity and (f) external quantum efficiency of the device varies with the excitation wavelength. (g) When $P/\Delta P_D = 30$, the relationship between the current retention factor of the device and the excitation wavelength. (h) The maximum enhancement factor of the device's various process currents when excited by different wavelengths of light within the range of $P/\Delta P_D$ = 0–30. (i) The photocurrent responsivity of Si/ZnO heterojunction self-powered PDs. (Ref 1–Ref 9 corresponds to preliminary experimental data of the devices with the same structure [26, 29, 33, 47–51], where blue (red) represents the condition without (with) background light in this work). The error bar is obtained from the 5 data.

$$\eta'' = R'_0/R'_{30} \tag{7}$$

where R'_0 and R'_{30} are the relative photocurrent responsivity of the device when the background light power density is 0 and 30 times the excitation light intensity, respectively. The $\eta''_{tt'}$, $\eta''_{ts'}$, $\eta''_{st'}$ and $\eta''_{ss'}$ are the retention factor of the device's $R'_{tt'}$, $R'_{ts'}$, $R'_{ss'}$ and $R'_{st'}$, respectively. Under 530, 660 and 970 nm light excitation, the device's $\eta''_{tt'}$ are 0.61, 0.59 and 0.61, respectively, which are 41.9%, 22.9% and 68.1% higher than the device's $\eta''_{ss'}$, respectively (Fig. 3(g)). The device's $\eta''_{tt'}$, $\eta''_{ts'}$ and $\eta''_{st'}$ are less affected by the excitation wavelength, and gradually decrease from 0.62, 0.58 and 0.65 with the increase of the excitation wavelength, and then remain stable. However, the device's $\eta''_{ss'}$ is significantly influenced by the excitation wavelength, and when the wavelengths are 365 and 970 nm, the corresponding $\eta''_{ss'}$ are 0.6 and 0.36, respectively. The thermal effect during excitation gradually increases as the excitation light's wavelength increases. The thermal effect has little effect on the transient current response of the device, but significantly affects the steady-state current response of the device [28]. This causes a decrease in the anti-interference ability of the device's steady-state current. Therefore, the device's enhancement factor $\alpha'_{tt'}$, $\alpha'_{ts'}$ and $\alpha'_{st'}$ (the definition of corresponding parameters under the condition of background light can be found in part C in the ESM) monotonically increases with the increase of excitation light wavelength (Fig. 3(h)). When the excitation wavelength is 970 nm, the device's $\alpha'_{tt'}$, $\alpha'_{ts'}$ and $\alpha'_{st'}$ is 8.33, 4.67 and 4.65, respectively. The n-Si/n-ZnO heterojunction device has a high photocurrent responsivity (both blue and red pentagrams) via using the device's transient photocurrent as the detection signal (Fig. 3(i)). Under the excitation of 365, 530, 660 and 970 nm wavelength light, the device's maximum responsivity under background light (red pentagrams) are 68.6, 428.8, 601.5 and 621.7 mA·W⁻¹, respectively. It has the highest photocurrent responsivity among the same type of PDs (Table S3 in the ESM) [26, 29, 33, 47–51].

To understand the large linear factor and LDR of the device's transient current, the distribution of photo-generated electrons and holes in the depletion region of the device and the energy band diagram of the device at the moment of 530 nm light excitation are shown in Fig. 4(a). According to the energy level positions of ZnO and Si (Fig. 1(c)), an internal electric field directed from Si to ZnO is formed at the n-Si/n-ZnO interface. Defect state energy levels are formed in the bandgap of ZnO as a result of the abundant defect

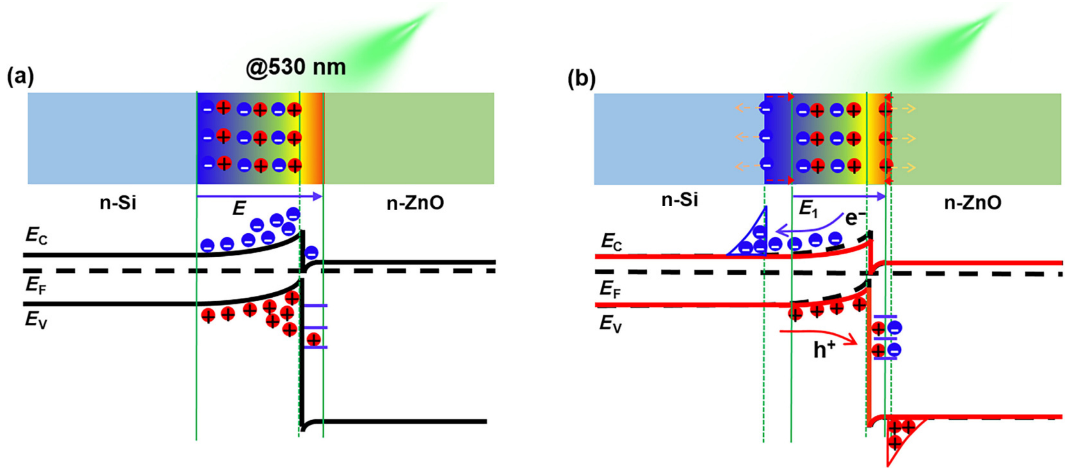

Figure 4 (a) At the moment of 530 nm light excitation, the depletion layer, carrier distribution and energy band diagram of the device. (b) The process of transitioning from a non-equilibrium state to a new equilibrium state is driven by an internal electric field, the depletion layer, carrier distribution and the energy band diagram of the device (E_C, E_F and E_V are the conduction band, Fermi level and valence band of semiconductor materials, respectively).

states in ZnO materials. At the moment of 530 nm light excitation, the photo-generated electron–hole pairs in the depletion layer are separated under the driving force of the built-in electric field E. Driven by the built-in electric field, photo-generated electrons will transport through n-Si material to the Au electrode, while photo-generated holes will transport from Si material to the n-Si/n-ZnO interface. The device's photo-generated electrons and holes are currently in a non-equilibrium state. Transient current is generated in the external circuit due to the transport of photo-generated electrons during the transition from a non-equilibrium state to a new dynamic equilibrium in the n-Si/n-ZnO heterojunction device when excited by light. At this point, the charge carriers within the device have not yet formed a stable distribution. The electric field generated by the steady-state photovoltaic effect (opposite to the built-in electric field direction) has not yet formed, and the equivalent built-in electric field of the device is relatively large, which can effectively drive the separation of photo-generated electrons and holes. Therefore, the LDR of the transient current of the device is relatively large and the linear factor is close to 1.

As the illumination time increases, the photo-generated carrier distribution in the device reaches equilibrium through transport and recombination. Due to the stable and exponential distribution of charge carriers in the neutral region of the material, an electric field opposite the direction of the built-in electric field is generated, weakening the magnitude of the built-in electric field (Fig. 4(b)). At this time, the equivalent built-in electric field is E_1 ($E_1 < E$), and the current response of the external circuit is the steady-state current I_s ($I_t > I_s$). Due to the monotonic decrease of E_1 with the increase of excitation light power density, the separation efficiency of photo-generated carriers in the device decreases, thereby reducing the photocurrent response of the device. Within a certain power range, the size of E is almost unaffected by the excitation luminescence power density and the capture probability of photo-generated carriers by interface states is relatively small. Therefore, compared to the device's I_s, the device's I_t has better linearity and larger LDR with increasing power density (Figs. 2(a) and 2(f)). The number of photo-generated carriers generated in the depletion region increases with the increase of excitation light power density, resulting in a decrease in the separation efficiency of photo-generated carriers driven by the built-in electric field E. Additionally, as the excitation light power density increases, the recombination probability of photo-generated charge carriers also increases. The combined effect of the above two causes the device's I_t to gradually deviate from linearity as the excitation light power density further increases.

The above research results indicate that using transient current as a detection signal can improve the LDR and anti-interference ability of the device. Therefore, transient current responsive devices have broad application potential in optoelectronic imaging. Figure 5(a) shows the schematic diagram of the imaging of the digital "6" under 530 nm wavelength light excitation using a 6 × 6 detector array. Measure devices' photocurrent response one by one using an ammeter (the prepared devices are shown in the illustration in Fig. 5(b)). Figure 5(b) shows the array device's current variation with power density. The device's I_t increases linearly with the optical power density and responds with good consistency, demonstrating that using the device's I_t can effectively perform optoelectronic imaging of images. However, as the optical power density rises, the device's I_s exhibits poor linear response, and the steady-state photocurrent variations of various devices are substantial, which is not advantageous for the photoelectric detection of images (Fig. S16(a) in the ESM). The device's β are all greater than 0.95 and 91.7% of devices' β in the range of 0.97–1.0, this indicates that the array device has good linearity in the photoelectric current response (Fig. 5(c)). 75% of devices' α_t larger than 100 indicates that using transient current I_t significantly improves the device's photoelectric current response (Fig. S16(b) in the ESM). Without background light, the response characteristics of the device's entire array of photocurrent imaging when 110.5 μW·cm^{-2}, 530 nm wavelength light is excited with the number "6" (Fig. 5(d)). Although the device's I_s imaging can roughly distinguish the contour of the number "6" the corresponding resolution is extremely low (Fig. 5(e)). Using the device's I_t imaging can clearly distinguish the number "6" (Fig. 5(f)). The distribution map of light power density with the number "6" in the case of background light (Fig. 5(g)), where the light power densities with lower brightness and higher brightness are 231.9 and 462.6 μW·cm^{-2}, respectively. The device's I_s imaging is completely unable to detect the number "6" in the presence of background light (Fig. 5(h)), whereas I_t imaging can better distinguish the number "6" (Fig. 5(i)). To better demonstrate the imaging quality of array devices, the optical power density has been increased from 1.2 to 3411.4 μW·cm^{-2} divided into 17 steps and the number "6" as shown in Fig. S17(a) in the ESM. The device's I_s

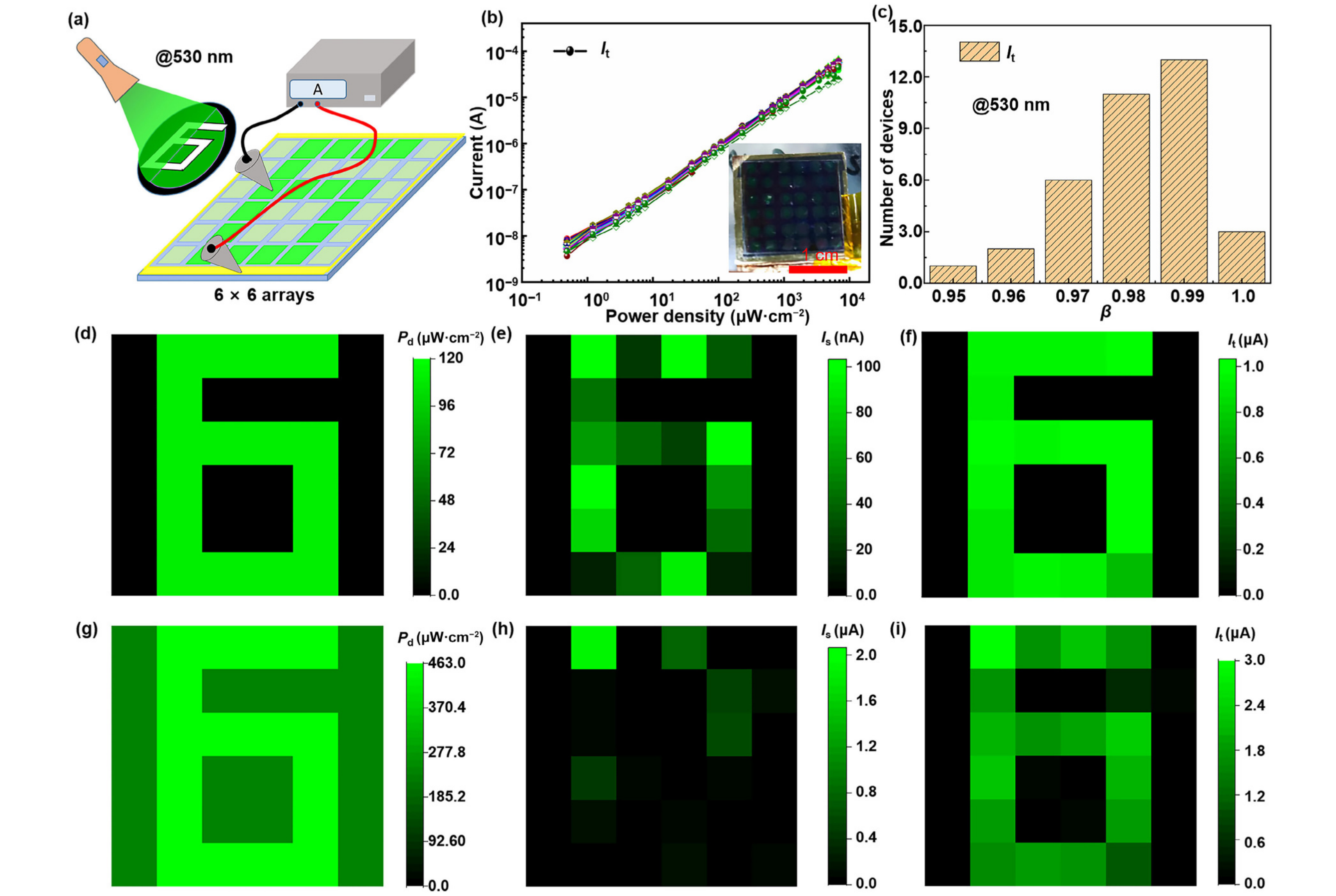

Figure 5 (a) Measurement schematic diagram of 6 × 6 PD array. (b) The relationship curve between the array devices' I_t and the optical power density. (c) The statistical diagram of the linear response factor of the PD array current I_t. (d) The light intensity distribution map of the number "6" under no background light conditions (P_d is the power density of the detection light). ((e) and (f)) The I_s and I_t imaging maps of the device. (g) The light intensity distribution map of the number "6" under the illumination background. ((h) and (i)) The I_s and I_t imaging maps of the device.

imaging cannot distinguish the stepped variations in light intensity (Fig. S17(b) in the ESM), whereas I_t imaging can better distinguish the variations in light power density (Fig. S17(c) in the ESM). The above research results indicate that using devices' I_t imaging can significantly improve the light-detecting sensitivity and imaging quality of devices.

4 Conclusion

By using the transient current generated by the device during optical switching as the detection signal, in this article we build an n-Si/n-ZnO heterojunction structure self-powered PD, greatly enhancing the photoelectric current responsivity and LDR of the PD. Under 365, 530, 660 and 970 nm light excitation, the device's maximum $R_{tt'}$ values are 89.3, 341, 439 and 542 mA·W^{-1}, respectively. These values are 6.6, 15.6, 9.7 and 7.5 times higher than R_s, respectively. The device's LDR is 113.8, 112.5, 105.9 and 74.6 dB, which are 25.9, 29.9, 20.3 and 14.4 dB higher than I_s, respectively. The research results on the influence of ambient light on the photoelectric response characteristics of devices indicate that the device's transient current response has a higher resolution of light intensity changes and resistance to light intensity interference. The research results of 6 × 6-array PDs for imaging 530 nm light show that using the device's I_t as the detection signal significantly improves the imaging quality and resolution of the device. This work provides new ideas for improving the responsiveness and LDR of self-powered PDs, and will promote the development and application of transient current responsive self-powered PDs in fields like high-sensitivity detection and rapid imaging.

Electronic supplementary material: Supplementary material (characterization of material properties, such as absorption of ZnO and Si and XRD spectra of ZnO; definition of device dynamic response process; the dynamic photoelectric response characteristics of the device in the absence and presence of background light conditions; the relationship curve between device response time and power density; the photoelectric response characteristics of array devices) is available in the online version of this article at https://doi.org/10.26599/NR.2025.94907007.

Data availability

All data needed to support the conclusions in the paper are presented in the manuscript and/or the Electronic Supplementary Material. Additional data related to this paper may be requested from the corresponding author upon request.

Acknowledgements

The authors thank the National Natural Science Foundation of China (No. 61974040), Special funds for scientific and technological research and development in Henan Province (No. 222300420116) and Key scientific research projects plan of colleges and universities in Henan Province (No. 21A140008) for financial support.

Declaration of competing interest

All the contributing authors report no conflict of interests in this work.

Author contribution statement

Y. L. Z.: Data curation, validation, writing manuscript, experimental design, funding acquisition. X. F.: Validation, experimental design. F. Y.: Project administration, funding acquisition. Y. F. D., Y. W. Z., T. C., and P. W.: Experiment assistance. J. M. G. and Z. L. D.: Theoretical discussion. G. C.: Project administration, experimental design, funding acquisition, manuscript revision, theoretical discussion. All the authors have approved the final manuscript.

Use of AI statement

None.

References

[1] Mennel, L.; Symonowicz, J.; Wachter, S.; Polyushkin, D. K.; Molina-Mendoza, A. J.; Mueller, T. Ultrafast machine vision with 2D material neural network image sensors. *Nature* **2020**, *579*, 62–66.

[2] Zhang, W. Q.; Gao, B.; Tang, J. S.; Yao, P.; Yu, S. M.; Chang, M. F.; Yoo, H. J.; Qian, H.; Wu, H. Q. Neuro-inspired computing chips. *Nat. Electron.* **2020**, *3*, 371–382.

[3] Zhang, Z. H.; Wang, S. Y.; Liu, C. S.; Xie, R. Z.; Hu, W. D.; Zhou, P. All-in-one two-dimensional retinomorphic hardware device for motion detection and recognition. *Nat. Nanotechnol.* **2022**, *17*, 27–32.

[4] Ma, N.; Zhang, K. W.; Yang, Y. Photovoltaic-pyroelectric coupled effect induced electricity for self-powered photodetector system. *Adv. Mater.* **2017**, *29*, 1703694.

[5] Peng, W. B.; Wang, X. F.; Yu, R. M.; Dai, Y. J.; Zou, H. Y.; Wang, A. C.; He, Y. N.; Wang, Z. L. Enhanced performance of a self-powered organic/inorganic photodetector by pyro-phototronic and piezo-phototronic effects. *Adv. Mater.* **2017**, *29*, 1606698.

[6] Xie, C.; Mak, C.; Tao, X. M.; Yan, F. Photodetectors based on two-dimensional layered materials beyond graphene. *Adv. Funct. Mater.* **2017**, *27*, 1603886.

[7] Jayachandran, D.; Oberoi, A.; Sebastian, A.; Choudhury, T. H.; Shankar, B.; Redwing, J. M.; Das, S. A low-power biomimetic collision detector based on an in-memory molybdenum disulfide photodetector. *Nat. Electron.* **2020**, *3*, 646–655.

[8] Wang, Y. F.; Zhu, Y.; Gu, H. M.; Wang, X. F. Enhanced performances of n-ZnO nanowires/p-Si heterojunctioned pyroelectric near-infrared photodetectors via the plasmonic effect. *ACS Appl. Mater. Interfaces* **2021**, *13*, 57750–57758.

[9] Meng, J. P.; Li, Q.; Huang, J.; Pan, C. F.; Li, Z. Self-powered photodetector for ultralow power density UV sensing. *Nano Today* **2022**, *43*, 101399.

[10] Wang, L.; Xue, H. Y.; Zhu, M.; Gao, Y. J.; Wang, Z. N. Graded strain-enhanced pyro-phototronic photodetector with a broad and plateau band. *Nano Energy* **2022**, *97*, 107163.

[11] Gong, X.; Tong, M. H.; Xia, Y. J.; Cai, W. Z.; Moon, J. S.; Cao, Y.; Yu, G.; Shieh, C. L.; Nilsson, B.; Heeger, A. J. High-detectivity polymer photodetectors with spectral response from 300 nm to 1450 nm. *Science* **2009**, *325*, 1665–1667.

[12] Ohta, J. *Smart CMOS Image Sensors and Applications*; 2nd ed. CRC Press: Boca Raton, 2020.

[13] Liao, F. Y.; Zhou, Z.; Kim, B. J.; Chen, J. W.; Wang, J. L.; Wan, T. Q.; Zhou, Y.; Hoang, A. T.; Wang, C.; Kang, J. F. et al. Bioinspired in-sensor visual adaptation for accurate perception. *Nat. Electron.* **2022**, *5*, 84–91.

[14] Liba, O.; Murthy, K.; Tsai, Y. T.; Brooks, T.; Xue, T. F.; Karnad, N.; He, Q. R.; Barron, J. T.; Sharlet, D.; Geiss, R. et al. Handheld mobile photography in very low light. *ACM Trans. Graph.* **2019**, *38*, 164.

[15] Kim, M.; Lee, G. J.; Choi, C.; Kim, M. S.; Lee, M.; Liu, S. Y.; Cho, K. W.; Kim, H. M.; Cho, H.; Choi, M. K. et al. An aquatic-vision-inspired camera based on a monocentric lens and a silicon nanorod photodiode array. *Nat. Electron.* **2020**, *3*, 546–553.

[16] Rao, Z. L.; Lu, Y. T.; Li, Z. W.; Sim, K.; Ma, Z. Q.; Xiao, J. L.; Yu, C. J. Curvy, shape-adaptive imagers based on printed optoelectronic pixels with a kirigami design. *Nat. Electron.* **2021**, *4*, 513–521.

[17] Hong, S.; Choi, S. H.; Park, J.; Yoo, H.; Oh, J. Y.; Hwang, E.; Yoon, D. H.; Kim, S. Sensory adaptation and neuromorphic phototransistors based on $CsPb(Br_{1-x}I_x)_3$ perovskite and MoS_2 hybrid structure. *ACS Nano* **2020**, *14*, 9796–9806.

[18] Xie, D. D.; Wei, L. B.; Xie, M.; Jiang, L. Y.; Yang, J. L.; He, J.; Jiang, J. Photoelectric visual adaptation based on 0D-$CsPbBr_3$-quantum-dots/2D-MoS_2 mixed-dimensional heterojunction transistor. *Adv. Funct. Mater.* **2021**, *31*, 2010655.

[19] He, Z. H.; Shen, H. G.; Ye, D. K.; Xiang, L. Y.; Zhao, W. R.; Ding, J. M.; Zhang, F. J.; Di, C. A.; Zhu, D. B. An organic transistor with light intensity-dependent active photoadaptation. *Nat. Electron.* **2021**, *4*, 522–529.

[20] Dou, L. T.; Yang, Y. M.; You, J. B.; Hong, Z. R.; Chang, W. H.; Li, G.; Yang, Y. Solution-processed hybrid perovskite photodetectors with high detectivity. *Nat. Commun.* **2014**, *5*, 5404.

[21] Bao, C. X.; Chen, Z. L.; Fang, Y. J.; Wei, H. T.; Deng, Y. H.; Xiao, X.; Li, L. L.; Huang, J. S. Low-noise and large-linear-dynamic-range photodetectors based on hybrid-perovskite thin-single-crystals. *Adv. Mater.* **2017**, *29*, 1703209.

[22] van Breemen, A. J. J. M.; Ollearo, R.; Shanmugam, S.; Peeters, B.; Peters, L. C. J. M.; van de Ketterij, R. L.; Katsouras, I.; Akkerman, H. B.; Frijters, C. H.; Di Giacomo, F. et al. A thin and flexible scanner for fingerprints and documents based on metal halide perovskites. *Nat. Electron.* **2021**, *4*, 818–826.

[23] Kim, C. O.; Kim, S.; Shin, D. H.; Kang, S. S.; Kim, J. M.; Jang, C. W.; Joo, S. S.; Lee, J. S.; Kim, J. H.; Choi, S. H. et al. High photoresponsivity in an all-graphene p-n vertical junction photodetector. *Nat. Commun.* **2014**, *5*, 3249.

[24] Shang, H. M.; Gao, F.; Dai, M. J.; Hu, Y. X.; Wang, S.; Xu, B.; Wang, P.; Gao, B.; Zhang, J.; Hu, P. A. Light-induced electric field enhanced self-powered photodetector based on van der waals heterojunctions. *Small Methods* **2023**, *7*, 2200966.

[25] Zhang, Y. W.; Shen, W.; Wu, S.; Tang, W. J.; Shu, Y. T.; Ma, K. K.; Zhang, B. T.; Zhou, P.; Wang, S. High-speed transition-metal dichalcogenides based schottky photodiodes for visible and infrared light communication. *ACS Nano* **2022**, *16*, 19187–19198.

[26] Dai, R. M.; Liu, Y.; Wu, J. F.; Wan, P.; Zhu, X. Z.; Kan, C. X.; Jiang, M. M. Self-powered ultraviolet photodetector based on an n-ZnO:Ga microwire/p-Si heterojunction with the performance enhanced by a pyro-phototronic effect. *Opt. Express* **2021**, *29*, 30244–30258.

[27] Panwar, V.; Nandi, S.; Majumder, M.; Misra, A. Self-powered ZnO-based pyro-phototronic photodetectors: Impact of heterointerfaces and parametric studies. *J. Mater. Chem. C* **2022**, *10*, 12487–12510.

[28] Zhang, Y. L.; Yang, F.; Guo, Q. W.; Feng, X.; Duan, Y. F.; Guo, J. M.; Cheng, G.; Du, Z. L. The self-powered photodetector of n-Si/n-ZnO heterojunction with enhanced temperature adaptability via transient current response. *J. Phys. D: Appl. Phys.* **2022**, *55*, 504004.

[29] Wang, Z. N.; Yu, R. M.; Wang, X. F.; Wu, W. Z.; Wang, Z. L. Ultrafast response p-Si/n-ZnO heterojunction ultraviolet detector based on pyro-phototronic effect. *Adv. Mater.* **2016**, *28*, 6880–6886.

[30] Wang, Y.; Zhu, L. P.; Feng, Y. J.; Wang, Z. N.; Wang, Z. L. Comprehensive pyro-phototronic effect enhanced ultraviolet detector with ZnO/Ag schottky junction. *Adv. Funct. Mater.* **2019**, *29*, 1807111.

[31] Zou, H. Y.; Dai, G. Z.; Wang, A. C.; Li, X. G.; Zhang, S. L.; Ding, W. B.; Zhang, L.; Zhang, Y.; Wang, Z. L. Alternating current photovoltaic effect. *Adv. Mater.* **2020**, *32*, 1907249.

[32] Feng, Y. J.; Zhang, Y. L.; Wang, Y.; Wang, Z. N. Frequency response characteristics of pyroelectric effect in p-n junction UV detectors. *Nano Energy* **2018**, *54*, 429–436.

[33] Zhang, Y. L.; Hu, M. N.; Wang, Z. N. Enhanced performances of p-si/n-ZnO self-powered photodetector by interface state modification and pyro-phototronic effect. *Nano Energy* **2020**, *71*, 104630.

[34] Yin, B.; Zhang, H. Q.; Qiu, Y.; Luo, Y. M.; Zhao, Y.; Hu, L. Z. The light-induced pyro-phototronic effect improving a ZnO/NiO/Si heterojunction photodetector for selectively detecting ultraviolet or visible illumination. *Nanoscale* **2017**, *9*, 17199–17206.

[35] Ouyang, B. S.; Zhang, K. W.; Yang, Y. Photocurrent polarity controlled by light wavelength in self-powered ZnO nanowires/SnS photodetector system. *iScience* **2018**, *1*, 16–23.

[36] You, D. T.; Xu, C. X.; Zhang, W.; Zhao, J.; Qin, F. F.; Shi, Z. L. Photovoltaic-pyroelectric effect coupled broadband photodetector in self-powered ZnO/ZnTe core/shell nanorod arrays. *Nano Energy* **2019**, *62*, 310–318.

[37] Kumar, M.; Patel, M.; Kim, J.; Lim, D. Enhanced broadband photoresponse of a self-powered photodetector based on vertically grown SnS layers via the pyro-phototronic effect. *Nanoscale* **2017**, *9*, 19201–19208.

[38] Dong, J. Q.; Wang, Z. J.; Wang, X. F.; Wang, Z. L. Temperature dependence of the pyro-phototronic effect in self-powered p-Si/n-ZnO nanowires heterojuncted ultraviolet sensors. *Nano Today* **2019**, *29*, 100798.

[39] Aranovich, J. A.; Golmayo, D.; Fahrenbruch, A. L.; Bube, R. H. Photovoltaic properties of ZnO/CdTe heterojunctions prepared by spray pyrolysis. *J. Appl. Phys.* **1980**, *51*, 4260–4268.

[40] Sze, S. M. Citation classic—Physics of semiconductor-devices. *Curr. Cont. Eng. Technol. Appl. Sci.* **1982**, *1*, 28.

[41] Bera, A.; Basak, D. Role of defects in the anomalous photoconductivity in ZnO nanowires. *Appl. Phys. Lett.* **2009**, *94*, 163119.

[42] Sze, S. M.; Li, Y. M.; Ng, K. K. *Physics of Semiconductor Devices*; 4th ed. John Wiley & Sons: New York, 2021.

[43] Konstantatos, G.; Sargent, E. H. Nanostructured materials for photon detection. *Nat. Nanotech.* **2010**, *5*, 391–400.

[44] Wang, Z. N.; Yu, R. M.; Pan, C. F.; Li, Z. L.; Yang, J.; Yi, F.; Wang, Z. L. Light-induced pyroelectric effect as an effective approach for ultrafast ultraviolet nanosensing. *Nat. Commun.* **2015**, *6*, 8401.

[45] Dai, Y. J.; Wang, X. F.; Peng, W. B.; Xu, C.; Wu, C. S.; Dong, K.; Liu, R. Y.; Wang, Z. L. Self-powered Si/CdS flexible photodetector with broadband response from 325 to 1550 nm based on pyro-phototronic effect: An approach for photosensing below bandgap energy. *Adv. Mater.* **2018**, *30*, 1705893.

[46] Ma, J. K.; Chen, M. J.; Qiao, S.; Guo, S. Y.; Chang, J. L.; Fu, G. S.; Wang, S. F. A new approach for broadband photosensing based on Ag_2Se/Si heterojunction tuned by pyro-phototronic effect. *Nano Energy* **2023**, *107*, 108167.

[47] Ahmed, A. A.; Qahtan, T. F.; Hashim, M. R.; Nomaan, A. T.; Al-Hardan, N. H.; Rashid, M. Eco-friendly ultrafast self-powered p-Si/n-ZnO photodetector enhanced by photovoltaic-pyroelectric coupling effect. *Ceram. Int.* **2022**, *48*, 16142–16155.

[48] Wang, B. Y.; Zhu, Y.; Dong, J. Q.; Jiang, J.; Wang, Q.; Li, S. T.; Wang, X. F. Self-powered, superior high gain silicon-based near-infrared photosensing for low-power light communication. *Nano Energy* **2020**, *70*, 104544.

[49] Chen, L.; Wang, B. Y.; Dong, J. Q.; Gao, F. L.; Zheng, H. W.; He, M.; Wang, X. F. Insights into the pyro-phototronic effect in p-Si/n-ZnO nanowires heterojunction toward high-performance near-infrared photosensing. *Nano Energy* **2020**, *78*, 105260.

[50] Silva, J. P. B.; Vieira, E. M. F.; Gwozdz, K.; Kaim, A.; Goncalves, L. M.; MacManus-Driscoll, J. L.; Hoye, R. L. Z.; Pereira, M. High-performance self-powered photodetectors achieved through the pyro-phototronic effect in Si/SnO_x/ZnO heterojunctions. *Nano Energy* **2021**, *89*, 106347.

[51] Peng, W. B.; Pan, Z. J.; Li, F. P.; Cai, Y. H.; He, Y. N. Pyro-phototronic effect enhanced ZnO nanowire-based tri-layer heterojunction for visible light sensing and communication. *Nano Energy* **2020**, *78*, 105268.